Research Square

Preprints are preliminary reports that have not undergone peer review.
They should not be considered conclusive, used to inform clinical practice,
or referenced by the media as validated information.

Surface plasmon resonance (SPR)-based highly integrated optical fiber sensor for simultaneous detection of temperature, magnetic field, methane, relative humidity, voltage and hydrogen

Chao Liu

msm-liu@126.com

Northeast Petroleum University

Weiqiang Wang

Northeast Petroleum University

Jingwei Lv

Northeast Petroleum University

Famei Wang

Shenzhen Technology University

Jianxin Wang

Northeast Petroleum University

Wei Liu

Northeast Petroleum University

Qiang Liu

Northeast Petroleum University

Paul K. Chu

City University of Hong Kong

Research Article

Keywords: Multi-parameter, optical fiber, surface plasmon resonance

Posted Date: September 14th, 2026

DOI: https://doi.org/10.21203/rs.3.rs-10728588/v1

License: This work is licensed under a Creative Commons Attribution 4.0 International License.
Read Full License

Additional Declarations: No competing interests reported.

Surface plasmon resonance (SPR)-based highly integrated optical fiber sensor for simultaneous detection of temperature, magnetic field, methane, relative humidity, voltage and hydrogen

Chao Liu[1], Weiqiang Wang[1], Jingwei Lv[1], Famei Wang[2], Jianxin Wang[1], Wei Liu[1], Qiang Liu[1], Paul K. Chu[3]*

[1] School of Physics and Electronic Engineering, Northeast Petroleum University, Daqing 163318, China

[2] Shenzhen Key Laboratory of Ultra-Intense Laser and Advanced Material Technology, Center for Intense Laser Application Technology, and College of Engineering Physics, Shenzhen Technology University, Shenzhen 518118, China

[3] Department of Physics, Department of Materials Science and Engineering, and Department of Biomedical Engineering, City University of Hong Kong, Tat Chee Avenue, Kowloon, Hong Kong, China

** msm-liu@126.com (C. Liu)*

Abstract

Guided by industrial safety production, a six-parameter sensor capable of simultaneously detecting temperature (*T*), magnetic field (*H*), relative humidity (*RH*), voltage (*U*), methane (CH_4), and hydrogen (H_2) is designed. Based on the surface plasmon resonance (SPR) principle and using a 12-hole fiber as the substrate, gold films are coated on alternately arranged air holes, which are then filled with polydimethylsiloxane (PDMS), magnetic fluid (MF), cryptophane-A and ultraviolet-cured fluorosiloxane complex (Crypt-A/UVCFS), polyvinyl alcohol (PVA), E7 nematic liquid crystal (E7NLC), and palladium-tungsten trioxide (Pd-WO_3), respectively. This sensor has realized the integrated detection of six physical quantities for the first time in the field of optical fiber sensing, and has promising application prospects in monitoring scenarios where multiple elements change simultaneously, such as environmental monitoring, industrial production status detection, and geological exploration.

Keywords: Multi-parameter, optical fiber, surface plasmon resonance.

1 Introduction

In the industrial production process, methane and hydrogen often coexist in high-risk production environments with complex working conditions. Such environments are usually affected by multiple physical quantities such as temperature, humidity, electric field, and magnetic field. Once parameters such as temperature, electromagnetic effects, and the concentrations of methane, hydrogen and other gases exceed the safe range during production, it is very likely to cause major safety accidents and result in immeasurable losses. Therefore, it is of vital importance to carry out real-time monitoring of the above-mentioned physical quantities and gas parameters [1-4]. Most traditional sensors rely on electrochemical or semiconductor electrical components, which have electromagnetic properties themselves and can easily cause safety accidents such as explosions in high-risk environments. In contrast, sensors based on optical principles can effectively avoid such risks [5]. Optical fibers have the advantages of small size, strong corrosion resistance, high sensitivity, and the ability to realize remote distributed sensing, making them particularly suitable for detection work in high-risk and complex industrial environments [6]。

Among various fiber-optic sensing principles, surface plasmon resonance (SPR) offers distinct advantages in terms of ease of integration, enabling effective solutions for multi-parameter sensing problems [7]. As early as 1993, the Jorgensone team first reported a fiber-optic gas sensor based on SPR [8]. To date, the publicly reported multi-parameter SPR fiber-optic sensors can be broadly categorized into two types: The first type consists of longitudinal extension structures, where multiple single-parameter

sensors are connected in series via a cascaded configuration. For example, in 2024, Wu et al. designed a three-parameter cascaded sensor utilizing polydimethylsiloxane (PDMS), magnetic fluid (MF), and polyvinyl alcohol (PVA). However, such sensors suffer from high loss and low sensitivity [9]. The second type comprises transverse extension structures, where multi-parameter synchronous sensing is achieved by filling different regions of the optical fiber cross-section with sensitive materials. Although the fabrication process for these sensors is more complex, they can achieve superior sensing performance.

In 2025, we proposed a dual-parameter sensor based on coreless optical fiber, which improved the sensitivity by an order of magnitude [10]; in the same year, we also designed a four-parameter sensor based on 8-hole fiber PCF for the detection of temperature, magnetic field, voltage and relative humidity [11]. This research provides an effective idea for accurate detection in complex industrial environments, but there is still room for improvement. Therefore, combining our previous research foundation on SPR optical fiber sensors, we designed a new type of optical fiber sensor structure, which can simultaneously detect a total of 6 field quantities including temperature, magnetic field, relative humidity, voltage, methane and hydrogen.

This sensor is based on a 12-hole fiber polished on three sides, uses gold film as the plasmonic material, and adopts PDMS, MF, cryptophane-A and ultraviolet-cured fluorosiloxane complex (Crypt-A/UVCFS), PVA, E7 nematic liquid crystal (E7NLC), and palladium-tungsten trioxide (Pd-WO_3) as sensitive materials. Numerical analysis is carried out on the sensor based on the finite element method. The results show that the

sensor can realize simultaneous detection of six physical quantities, has excellent sensing performance, achieves a breakthrough in integration in the field of optical fiber sensing, and is applicable to high-risk complex monitoring scenarios.

2 Model and Theory

2.1 Model

Fig.1 shows the initial structural parameters of the sensor: the optical fiber diameter is 125 μm, the air hole diameter d = 15 μm, the distance from the air hole to the fiber core l_1 = 43.75 μm, the gold film thickness h = 40 nm, and the side polishing depth l_2 = 0.35d.

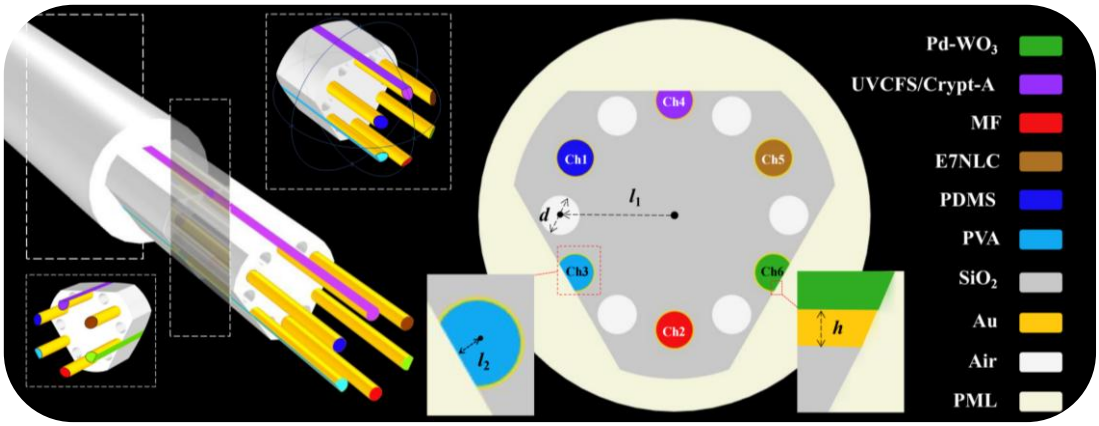


Fig. 1. Cross-sectional structure of the sensor.

The sensor can be prepared through the process shown in Fig2. First, a femtosecond laser (fs Laser) is used to drill holes on the coreless fiber (CF) [12], then a gold film is deposited in the alternately distributed air holes by chemical vapor deposition (CVD) [13], and three-sided polishing is performed on the optical fiber using the fs Laser. Finally, six types of sensitive materials are selectively filled using the sol-gel method

(SGM) [14].

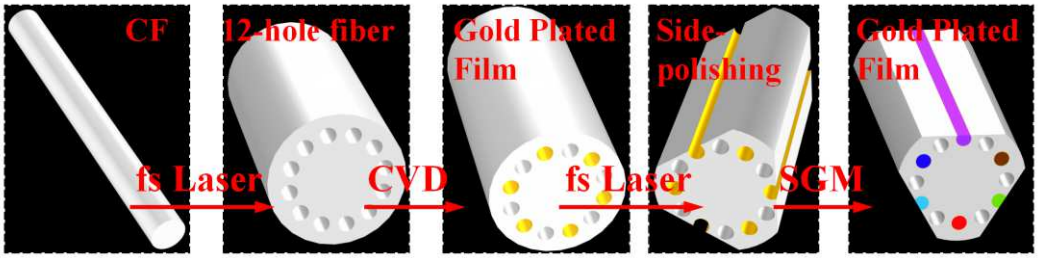


Fig. 2. Fabrication process of the 6-parameter sensor.

2.2 Theory

The substrate of this 6-parameter sensor is fused silica, and its refractive index (n) is affected by temperature, as expressed by the Sellmeier equation [15]:

$$n^2(\lambda,T) = 1.31552 + \mathrm{A}_1 T + \frac{(\mathrm{B}_1+\mathrm{B}_2 T)\lambda^2}{\lambda^2-(\mathrm{B}_3+\mathrm{B}_4 T)} + \frac{(\mathrm{C}_1+\mathrm{C}_2 T)\lambda^2}{\lambda^2-\mathrm{C}_3}, \quad (1)$$

where n is the refractive index of SiO_2, λ is the wavelength of the incident light, T is the ambient temperature, $A_1 = 6.90754\times10^{-6}$ °C^{-1}, $B_1 = 0.788404$, $B_2 = 2.35835\times10^{-5}$ °C^{-1}, $B_3 = 0.0110199$ μm^2, $B_4 = 0.584758\times10^{-6}$ °C$^{-1}\cdot$μm^2, $C_1 = 0.91316$, and $C_2 = 0.548368\times10^{-6}$ °C^{-1}, $C_3 = 100$ μm^2. Gold serves as the plasmonic medium to excite SPR, is used, and its dielectric constant can be derived by the Drude-Lorentz model:

$$\varepsilon_{\mathrm{Au}}(\omega) = \varepsilon_1 + \mathrm{i}\varepsilon_2 = \varepsilon_\infty - \frac{\omega_\mathrm{p}^2}{\omega(\omega+\mathrm{i}\omega_\mathrm{c})}, \quad (2)$$

where ε_1 and ε_2 are the real and imaginary parts of the metal dielectric constant, respectively, $\varepsilon_\infty = 9.48$ is the dielectric constant of gold at high frequencies, ω is the

angular frequency of the incident light, ω_p = 1.36×1016 rad/s represents the angular frequency of the plasma, and ω_c = 1.45×1014 rad/s represents the damping frequency [16].

Voltage sensing is achieved by placing E7NLC in the air holes. The n value of E7NLC is affected not only by the voltage, but also by the combined action of T and H [13], [14]. The influence can be calculated using Δn [17], [18]:

$$\Delta n=\frac{\Delta\varepsilon_0\Delta x_0 H^2}{9a_0(T-T^*)\sqrt{\bar{\varepsilon}}}, \tag{3}$$

where $\Delta\varepsilon_0$ is the anisotropy of the saturated dielectric, $\bar{\varepsilon}$ is the isotropic part of the dielectric constant.

The refractive index of E7NLC is mainly affected by U.

$$E_C\approx\frac{\pi}{d}\sqrt{\frac{K_{11}}{\Delta\varepsilon}},\ \theta=\begin{cases}0, U\le U_c\\ \frac{\pi}{2}-2\tan^{-1}\left[\exp\left(-\frac{U-U_c}{30U_c}\right)\right], U\ge U_c\end{cases}, \tag{4}$$

where E_C is the threshold electric field. Under the action of this electric field, the E7NLC molecules deflect by an angle of θ along the X-axis. $\Delta\varepsilon$ represents the difference in dielectric constants. Under an electric field with a frequency of 1 kHz, $\Delta\varepsilon$ = 12.7, k_{11} = 11.1pn (k_{11} is the splay elastic constant) [19], [20].

The refractive index of E7NLC can be summarized as the ordinary refractive index no, and the extraordinary refractive index, n_o and n_e can be calculated using the following Cauchy models [21]

$$\begin{cases} n_o = A_o + \left(\frac{B_o}{\lambda^2}\right) + \left(\frac{C_o}{\lambda^4}\right) \\ n_e = A_e + \left(\frac{B_e}{\lambda^2}\right) + \left(\frac{C_e}{\lambda^4}\right) \end{cases}, \quad \begin{cases} n_x = n_o \\ n_y = \left(\frac{\sin^2(\theta)}{n_e^2} + \frac{\cos^2(\theta)}{n_o^2}\right)^{-\frac{1}{2}} \end{cases}. \tag{5}$$

The influence of T on the refractive index of E7NLC is mainly reflected in the difference of Cauchy coefficients, where A_o, B_o, C_o, A_e, B_e, and C_e are the fitting coefficients of the Cauchy model. Under the combined effect, the calculation formula for the n-value of E7NLC is as follows [10]:

$$n_U = \sqrt{\frac{n_x^2 + n_y^2}{3}}, \qquad n_{E7NLC} = n_U + \Delta n. \tag{6}$$

MF is widely used in magnetic field detection. The movement of the magnetic nanoparticles is affected by the magnetic field, which in turn causes significant changes in the optical properties. In addition, changes in temperature affect the optical properties of MF. By applying the Langevin model, the refractive index of MF can be calculated (magnetic field range = 30–200 Oe.) [22]:

$$n_{MF} = (n_s - n_p)\left[\coth\left(\alpha \frac{H - H_{c,n}}{T}\right) - \frac{T}{\alpha(H - H_{c,n})}\right] + n_p, \tag{7}$$

where n_p = 1.4352 is the initial refractive index of MF, n_s = 1.4385 represents the saturated refractive index of MF, $H_{c,n}$= 30 Oe is the magnetic field threshold, and α = 5 is the fitting coefficient.

PVA is a humidity-sensitive material. PVA exhibits excellent sensitivity in the

relative humidity range between 10%RH and 90%RH. Since PVA contains hydrophilic hydroxyl groups, it expands after absorbing water, and the refractive index changes with *RH* according to the following equation (humidity range = 10%–90%) [23]:

$$n_{\mathrm{PVA}} = -3 \times 10^{-6} RH^2 - 10^{-4} RH + 1.4738 \ . \tag{8}$$

Compared with traditional temperature-sensitive materials such as toluene and ethanol, PDMS has a higher thermo-optic coefficient. Its applicable temperature range is -50-200 ºC. The refractive index of PDMS is affected only by temperature and exhibits a linear relationship with temperature as shown below [24]:

$$n_{\mathrm{PDMS}} = -4.5 \times 10^{-4} T + 1.4176. \tag{9}$$

The Crypt-A/UVCFS nanomembrane can rapidly absorb methane, and its reaction with methane is reversible. In the range of 0-2%, the refractive index of the methane sensor decreases linearly with methane concentration, as shown in the following:

$$n_{\mathrm{UVCFS/Crypt-A}} = 1.4478 - 0.0038c(\mathrm{CH_4}), \tag{10}$$

where $\boldsymbol{c}(\mathrm{CH_4})$ represents the concentration of methane gas [25], [26].

Pd-WO_3 is widely used in hydrogen detection due to the relatively fast adsorption. In the range of 0%-2%, the equation for the change of the refractive index of Pd-WO_3

with hydrogen concentration is expressed below (hydrogen concentration range = 0%-3%), as shown in the following [27]:

$$n_{\mathrm{Pd-WO_3}} = 1.995 - 0.00067c(\mathrm{H_2}), \tag{11}$$

where $c(H_2)$ represents the concentration of hydrogen gas.

To summarize, the multi-parameter optical fiber sensor can detect T, H, CH_4, RH, U, and H_2 simultaneously. By calculating the sensitivity of each channel (i = 1, 2, 3, 4, 5, 6) and using the sensitivity matrix, accurate calibration can be achieved. The specific formulas are as follows:

$$S_i(X) = \frac{\Delta\lambda_{\mathrm{peak}i}}{\Delta X} \text{ and} \tag{12}$$

$$\begin{bmatrix} \Delta RW_1 \\ \Delta RW_2 \\ \Delta RW_3 \\ \Delta RW_4 \\ \Delta RW_5 \\ \Delta RW_6 \end{bmatrix} = \begin{bmatrix} S_1(T) & S_1(H) & S_1(CH_4) & S_1(RH) & S_1(U) & S_1(H_2) \\ S_2(T) & S_2(H) & S_2(CH_4) & S_2(RH) & S_2(U) & S_2(H_2) \\ S_3(T) & S_3(H) & S_3(CH_4) & S_3(RH) & S_3(U) & S_3(H_2) \\ S_4(T) & S_4(H) & S_4(CH_4) & S_4(RH) & S_4(U) & S_4(H_2) \\ S_5(T) & S_5(H) & S_5(CH_4) & S_5(RH) & S_4(U) & S_5(H_2) \\ S_6(T) & S_6(H) & S_6(CH_4) & S_6(RH) & S_6(U) & S_6(H_2) \end{bmatrix} \begin{bmatrix} \Delta T \\ \Delta H \\ \Delta CH_4 \\ \Delta RH \\ \Delta U \\ \Delta H_2 \end{bmatrix}, \tag{13}$$

where $S_i(X)$ represents the sensitivity of the i^{th} (i = 1, 2, 3, 4, 5, 6) loss peak with respect to X (X representing T, H, CH_4, RH, U or H_2 respectively), ΔRW_i (i = 1, 2, 3, 4, 5, 6) denotes the offset of the i^{th} loss peak, and ΔT, ΔH, $\Delta c(CH_4)$, ΔRH, ΔU and $\Delta c(H_2)$ correspond to the variations of T, H, CH_4, RH, U and H_2 respectively.

The influence of noise computational errors on the inversion results is evaluated by

the matrix condition number as expressed below:

$$\mathrm{cond}(\mathrm{A}) = \|\mathrm{A}\| \cdot \|\mathrm{A}^{-1}\|, \tag{14}$$

where A denotes the sensitivity matrix in Equation (13), A^{-1} represents the inverse of matrix A, and cond(A) stands for the condition number of matrix A and denotes the matrix norm [28], [29].

The sharpness of the loss peak, an important metric to evaluate the optimization degree of the sensor, is calculated as follows:

$$SHP = \frac{Loss}{FWHM}\left(\frac{\mathrm{dB}}{\mu\mathrm{m}^2}\right), \tag{15}$$

where *SHP* is the sharpness of the loss peak and *FWHM* represents the full-width at half-maximum of the loss peak. The larger the *SHP*, the higher the resolution of the sensor.

When light waves propagate through total reflection inside the fiber core, the evanescent waves that penetrate into the metal film interact with internal free electrons to form surface plasmon polariton (SPP) waves. As shown in Equation (16), when the propagation constants (k) of the SPP mode and the fundamental mode (FM) at a specific wavelength match, the phase matching condition is satisfied, and SPR produces a surface plasmon resonance wave (SPW). SPR causes a loss peak at the resonance wavelength (*RW*) in the spectrum, and *RW* is affected by n near the metal film.

Therefore, by embedding sensitive materials into metal-plated optical fibers, various physical entities can be indirectly detected by analyzing the changes in *RW*. The loss of light waves can be calculated by Equation (17) [11]:

$$\frac{2\pi}{\lambda} n_{\text{core}} \sin\theta_i = \text{Re}\left(\frac{2\pi}{\lambda}\sqrt{\frac{\varepsilon_{\text{Au}} n_{\text{medium}}^2}{\varepsilon_{\text{Au}} + n_{\text{medium}}^2}}\right) = K_{\text{spw}}. \tag{16}$$

$$\alpha_{loss} = 8.686 \times \frac{2\pi}{\lambda} \text{Im}(n_{\text{eff}}) \times 10^7 \left(\frac{\text{dB}}{\text{cm}}\right), \tag{17}$$

where θ_i is the incident angle of the light wave, n_{core} is the refractive index of the fiber core, n_{medium} is the refractive index of the sensing material filling area, λ is the wavelength of the incident light, and Im(n_{eff}) is the imaginary part of the effective refractive index.

Fig. 3 shows the simulation results of the optical fiber waveguide mode based on COMSOL software. Although the refractive index of the sensitive materials is higher than that of the optical fiber, the air hole structure reduces the equivalent refractive index of the cladding region. Meanwhile, it is confirmed by multi-mode comparison that only the fundamental mode can be effectively confined and stably transmitted in the fiber core, so we select the fundamental mode as the object of sensing analysis. It verifies the feasibility of the sensing structure from the optical mechanism and ensures the clear identifiability of the multi-channel SPR resonance peaks.

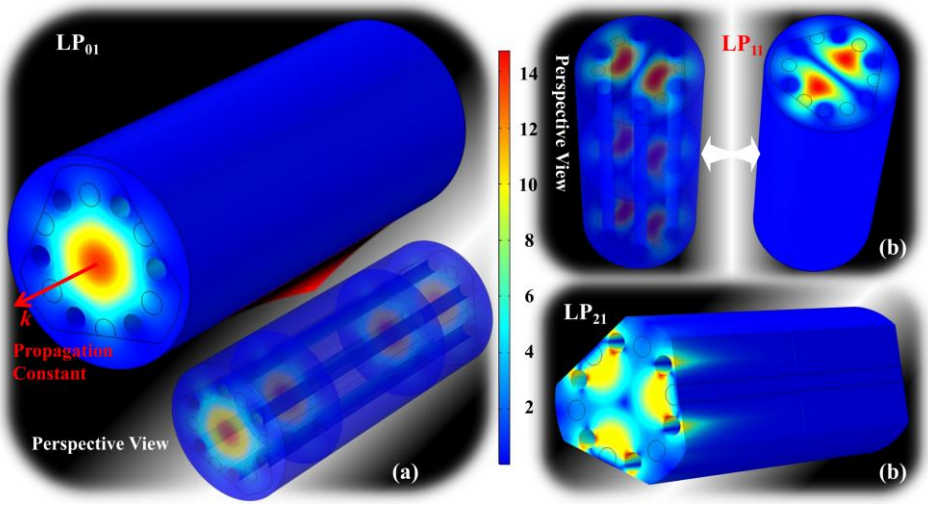


Fig. 3. (a)-(c) 3D electric field distribution diagram for the coupling between light waves and sensitive materials.

From the perspective of the interaction between light and matter, the influence of the electric field is significantly greater than that of the magnetic field. Therefore, we only need to analyze the electric field distribution of the sensor. Among the light wave modes propagating in the fiber core, the FM mode has the shortest cut-off wavelength, so analyzing the FM mode is conducive to subsequent signal analysis. By filling with sensing materials with different properties, the sensor does not have a rotational symmetry, and therefore, it is necessary to conduct a comparative analysis of the modal characteristics of x-pol FM and y-pol FM.

Fig.4 shows the spectral characteristics of the sensor with the initial structural parameters for T = 25 ºC, H = 60 Oe, $c(CH_4)$ = 1.5%, RH = 50%, U = 200V, and $c(H_2)$ = 0.75%. Fig. 4(a) presents the variation of the real part of the effective refractive index (n_{eff}) of the first-order SPP mode, the loss of the y-pol FM, and the real part of its n_{eff} with wavelength. Six distinct peak extrema are observed at wavelengths of 577 μm, 636

μm, 712 μm, 820 μm, 997 μm, and 1293 μm. In addition, the n_{eff} curves of the y-pol FM and the SPP mode intersect at the extreme points, indicating that the phase matching condition is satisfied at these 6 specific wavelengths, consequently exciting SPR. These 6 wavelengths are referred to as the resonance wavelengths (*RWi*, i = 1, 2, 3, 4, 5, 6). Fig. 4(b) compares the loss spectra of the x-pol FM and y-pol FM, revealing that the loss spectrum of x-pol FM changes relatively gently, making it unsuitable for spectral analysis. Fig. 4(c) shows the mode field diagrams of the x-pol FM, y-pol FM, and SPP mode at the resonance wavelengths. According to the modal distribution in the figure, the coupling conditions of the sensor can be compared.

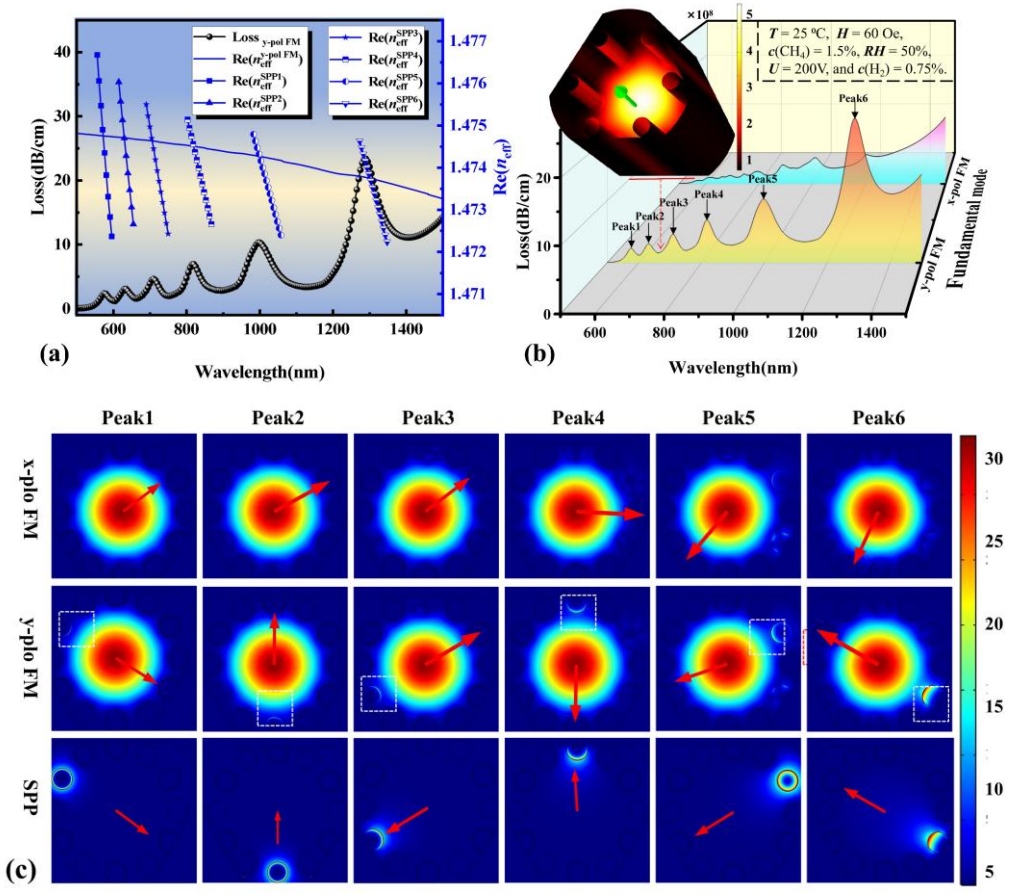


Fig. 4. (a) Loss spectra of the y-pol FM and Re(n_{eff}) for y-pol FM and SPP; (b) Loss spectra of the x-pol FM and y-pol FM; (c) Electric field distributions of x-pol FM, y-

pol FM, and SPP mode.

Ch1, Ch2, and Ch5 are filled with PDMS, MF, and E7NLC, respectively, making Ch1 sensitive to temperature, Ch2 sensitive to magnetic field, and Ch5 sensitive to voltage. UVCFS/Crypt-A, PVA, and Pd-WO_3 are deposited in Ch3, Ch4, and Ch6, respectively, making Ch3 sensitive to methane, Ch4 sensitive to humidity, and Ch6 sensitive to H_2. At *RW*1, the loss peak of the y-pol FM reaches the peak, and the electric field distribution of the y-pol FM tends to Ch1, indicating that at the *RW*1 wavelength, significant coupling occurs between the y-pol FM and the SPP mode, and the energy of the fiber core is coupled into Ch1. Therefore, the refractive index is detected by the offset of *RW*1 corresponding to SPR Peak1. The detection methods for *H*, CH_4, *RH*, *U*, and H_2 are similar. As shown in Fig. 5, when *T*, *H*, CH_4, *RH*, *U*, and H_2 change, the loss peaks of the y-pol FM loss spectrum shift. As shown in Fig. 5(a), when the other field quantities are constant, as *T* increases, Peak1 redshifts. Hence, Peak1 can uniquely detect the refractive index. Fig. 5(b) shows that only when *H* increases, Peak2 shows a significant blueshift, and so Peak2 can uniquely detect temperature. Similarly, according to Figs. 5(c), (d), (e), and (f), Peak3 can be used to detect CH_4, Peak4 for relative humidity, Peak5 for voltage, and Peak6 for H_2.

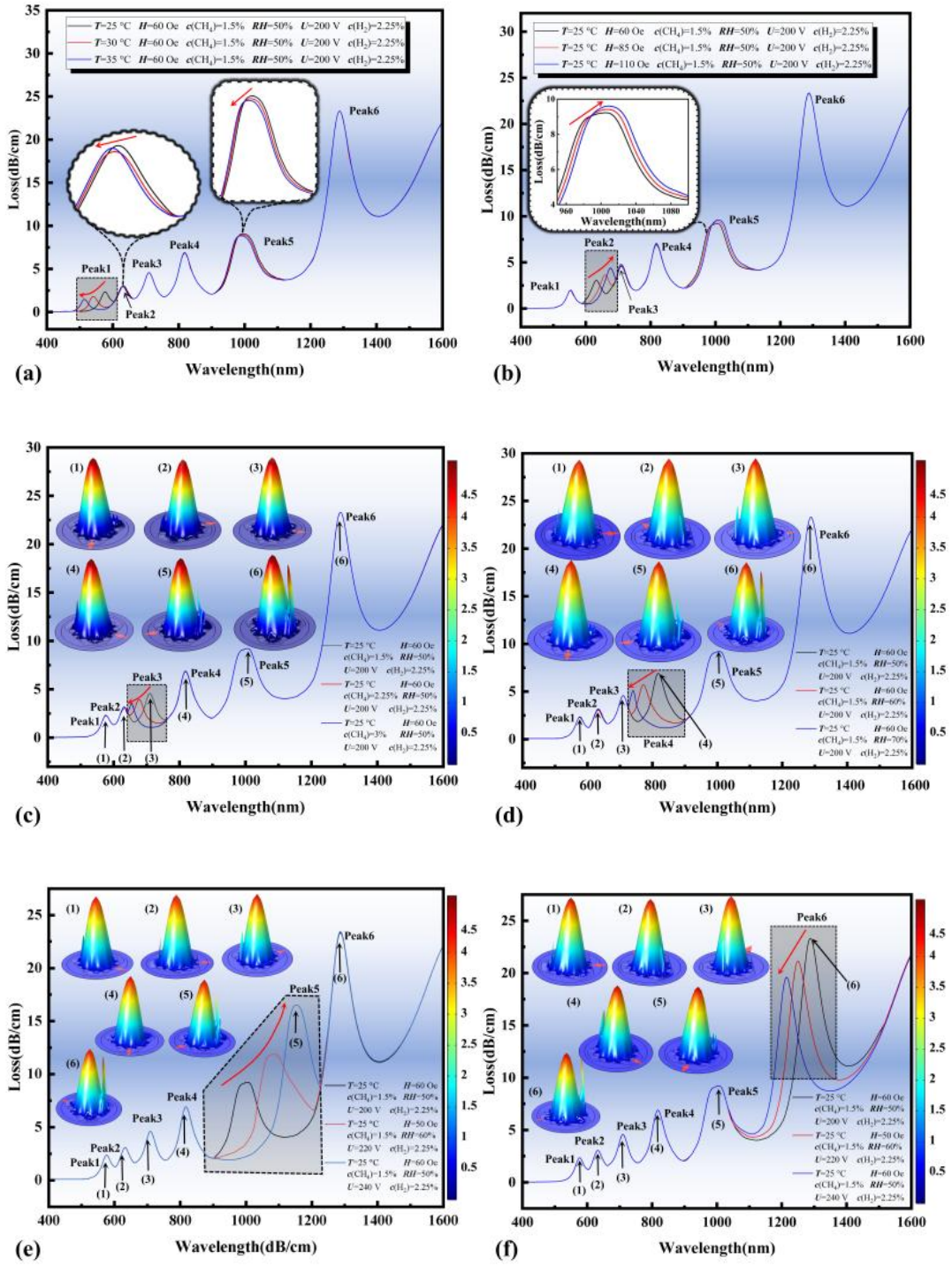


Fig. 5. (a)-(f) Relationship between the loss spectrum of y-pol FM and *T*, *H*, *c*(CH_4), *RH*, *U,* and *c*(H_2)

3 Structural Optimization

As shown in the loss spectra and electric fields in Fig. 5, the coupling degree of Peak1-6 is weak, resulting in poor sharpness of the loss peaks, which is unfavorable for the analysis of spectral signals. Therefore, the structure of the sensor is optimized. Optimization is carried out step by step from the inside of the fiber core outward, with the optimization sequence being d, l_1, and h. The cladding radius of the PCF is fixed at 125 μm, and l_1 is 0.25d. Since an increase in the sensitivity of one entity is accompanied by a decrease in the sensitivity of other field quantities, neither sensitivity nor the sensitivity-related figure of merit (FOM) is used as the optimization criterion. Optimization is based on 6 average sharpness (*AS*) values of the light wave loss peaks and the total loss (*SL*). The purpose of the optimization is to make the loss peaks sharper and reduce the total loss. Specifically, $SL = \sum_{i=1}^{6} lossi$ where *lossi* is the loss value of the *i*-th resonance peak. $AS = \frac{\sum_{i=1}^{6} S_{HPi}}{6}$, where *SHPi* is the sharpness of the *i*-th resonance peak. The larger the value of *AS*, the more accurate the sensor, whereas the smaller the *SL* value, the higher the transmission efficiency.

3.1 Optimization of Air Hole Radius

The optimization range of d is 11.25-21.25 μm. When d is less than 11.25 μm, the loss spectrum no longer exhibits 6 distinct peaks. If d exceeds 21.25 μm, the air hole spacing becomes too small, thus causing mechanical breakage during fiber drawing. Fig. 6(a) shows a comparison of the 3D models of the sensor for different d values. Fig. 6(b) compares the coupling effects by presenting the electric field distributions at 6 resonance wavelengths. Fig. 6(c) presents the y-pol FM loss spectra corresponding to

different d values. As d increases, the loss spectrum redshifts because when d increases, the effective n_{eff} of the fiber core decreases, which in turn reduces n_{eff} of the y-pol FM. According to the optical formulas $n = c/v$ and $\lambda = v/f$ (where c is the speed of light in vacuum, v is the speed of light in the medium, and f is the intrinsic frequency of light), the decrease in n_{eff} will cause an increase in wavelength λ, thus resulting in the redshift phenomenon. Fig. 6(d) summarizes the variation curves of *AS* and *SL* of the 6 loss peaks with d. When d = 18.25 μm, the average sharpness of the loss peaks reaches the maximum value, and the total loss is relatively small. After comprehensive evaluation, d is selected to be 18.25 μm.

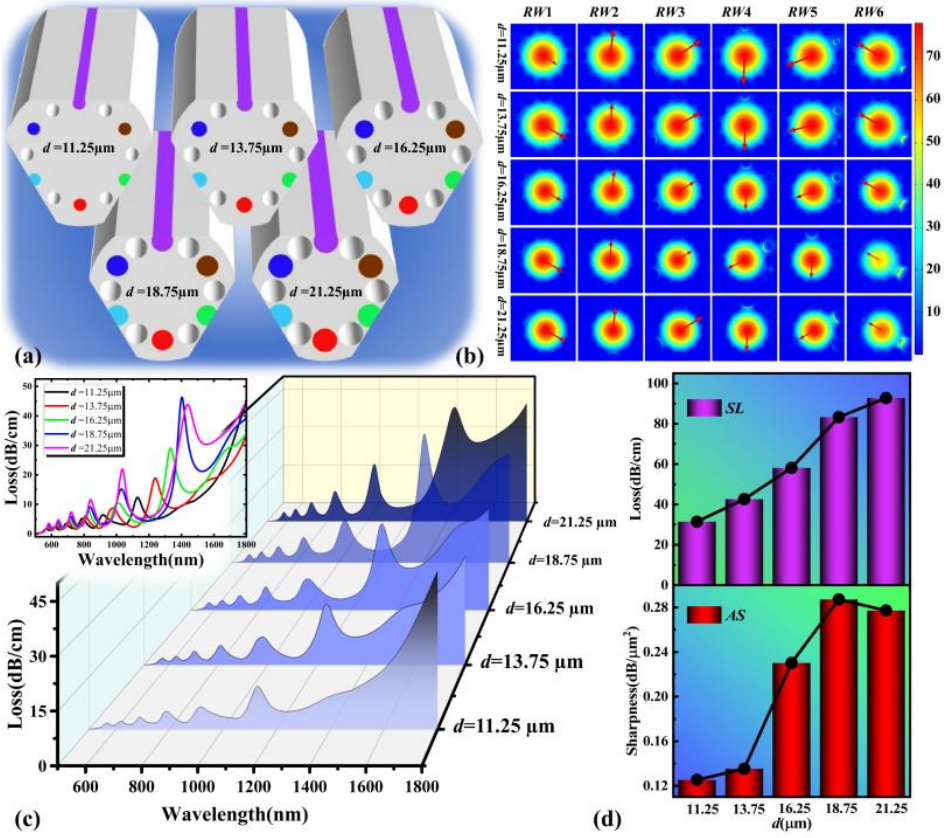


Fig. 6. (a) 3D models of the sensor, (b) Electric field distributions corresponding to the resonance wavelengths, (c) y-pol FM loss spectra, and (d) Variation curves of *AS* and *SL* of the loss spectra for d between 11.25 μm and 21.25 μm.

3.2 Optimization of Air Hole Position

When d is 18.25 μm, l_1 is optimized in the range of 37.5-50 μm. When l_1 is less than 37.5 μm, the air hole spacing is too small, leading to breakage. When l_1 exceeds 50 μm, the sensor no longer produces obvious loss peaks. Fig. 7(c) shows that as l_1 increases, the loss spectrum shows almost no shift. This is because the refractive index distribution of the fiber cross-section presents a fan-shaped distribution. When the air hole size is fixed but their positions move radially, the n difference between the fiber core and the filled region remains basically unchanged, resulting in no obvious shift in the loss spectrum. In addition, as l_1 decreases, the loss increases because a smaller l_1 shortens the distance between the gold film and the fiber core, making the y-pol FM and SPP modes more likely to couple for a greater loss. When l_1 is 40.625 μm, the average sharpness is relatively high, and the total loss is relatively low. Therefore, l_1 is determined to be 40.625 μm.

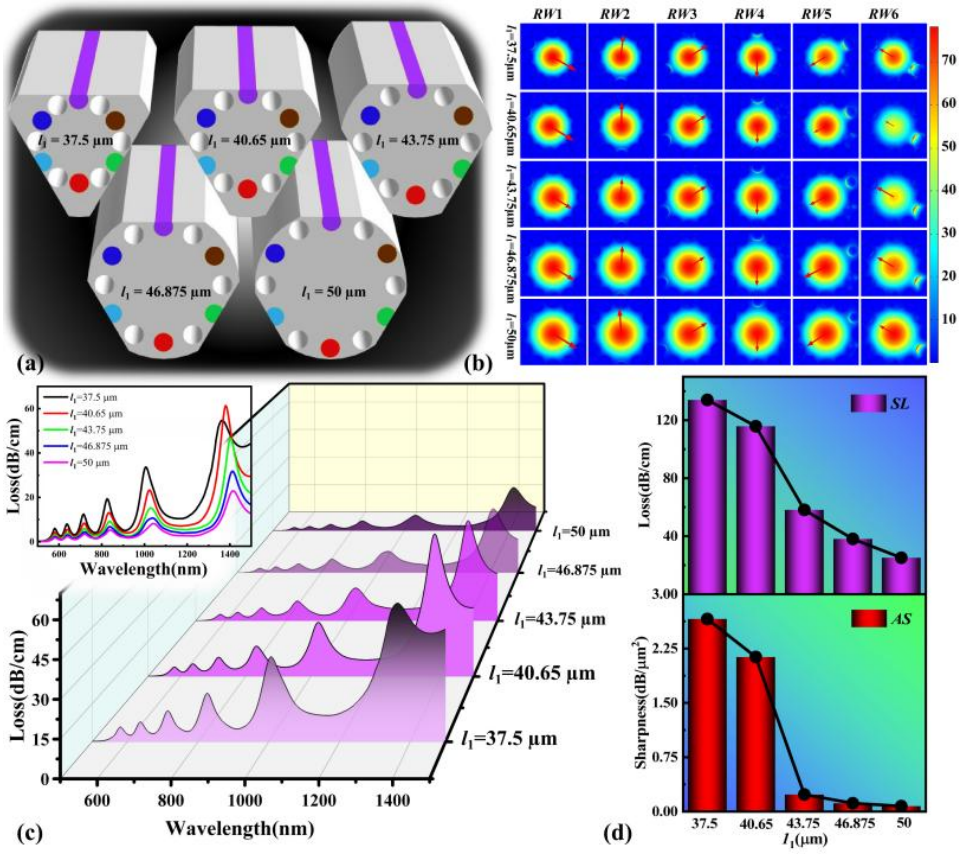


Fig. 7. (a) 3D models of the sensor, (b) Electric field distributions corresponding to the resonance wavelengths, (c) y-pol FM loss spectra, and (d) Variation curves of *AS* and *SL* of the loss spectra for l_1 between 37.5 μm and 50 μm.

3.3 Optimization of Gold film Thickness

When d is 18.25 μm and l_1 is 40.65 μm, h is optimized within the range of 20-50 nm. When h is less than 20 nm, film deposition becomes more difficult, and the sensor exhibits excessive loss. When h is greater than 50 nm, the sensor cannot excite obvious loss peaks. Fig. 8(c) shows that as h increases, the loss spectrum exhibits redshifts because a larger h reduces the refractive index near the gold film. As aforementioned, $v = c/n$ and $\lambda = v/f$, so an increase in λ leads to a redshift. When h = 25 nm, the average

sharpness of the loss spectrum is the highest, and the total loss is relatively low. After comprehensive consideration of various factors, *h* is chosen to be 25 nm.

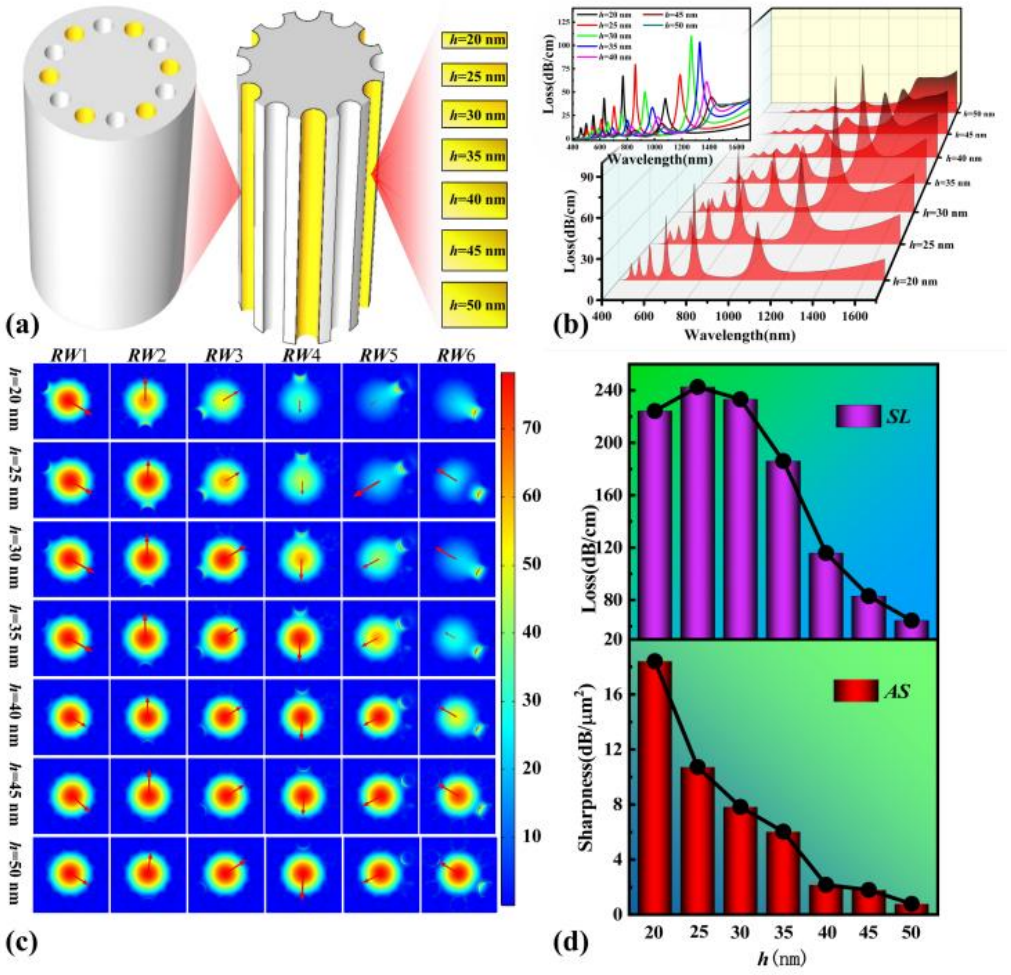


Fig. 8. (a) 3D models of the sensor, (b) Electric field distributions corresponding to the resonance wavelengths, (c) y-pol FM loss spectra, and (d) Variation curves of *AS* and *SL* of the loss spectra for *h* between 20 nm and 50 nm.

4. Results

The performance of the sensor can be evaluated by the experimental platform shown in Fig.9. Light emitted from the supercontinuum light source is transmitted to the

coupler through a single-mode optical fiber. One end of the coupler is connected to the sensor placed inside a control box, and the other end is connected to a spectrometer. After converting the optical signal into an electrical signal, the signal is transmitted to a computer for analysis.

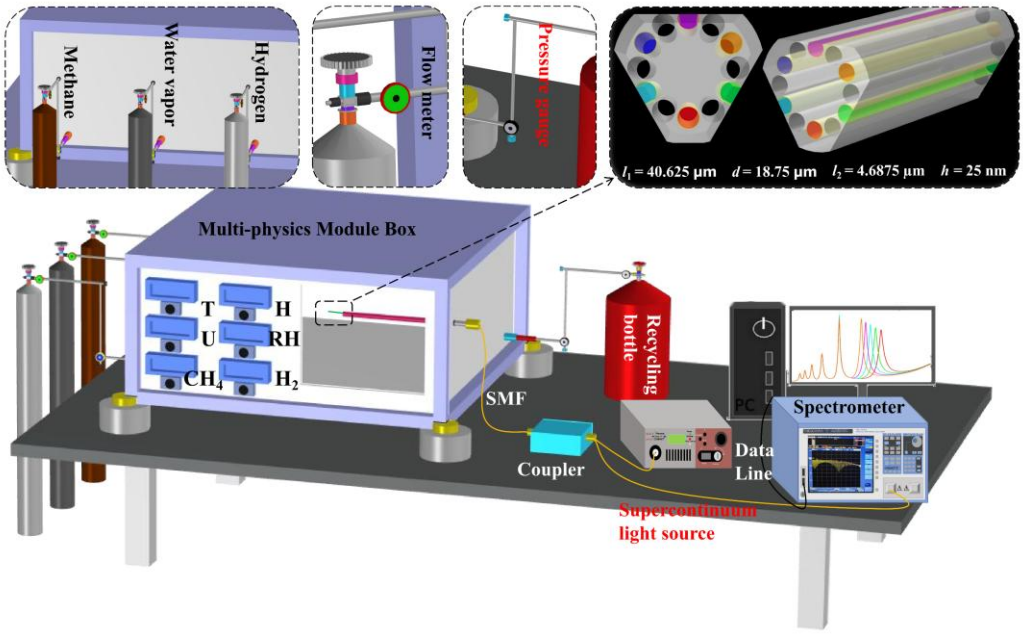


Fig. 9. Experimental setup for evaluating the sensing performance.

Fig.10(a) shows the temperature sensing characteristics of the optimized sensor. When the temperature varies in the range of 20 ºC-40 ºC, Peak 1 exhibits an obvious shift. Linear fitting is performed between the shift of each resonance peak and temperature, and the results are shown in Fig.11(a): $RW1$ = -4.9T + 618(nm) (R^2 = 99.8%); $RW2$ = -0.36T + 562(nm) (R^2 = 92.7%); $RW3$ = -0.063T + 711(nm) (R^2 = 99.93%); $RW4$ = -0.016T + 721(nm) (R^2 = 99.83%); $RW5$ = -0.64T + 876(nm) (R^2 = 92.7%); $RW6$ = -0.072T + 1198(nm) (R^2 = 99.76%).

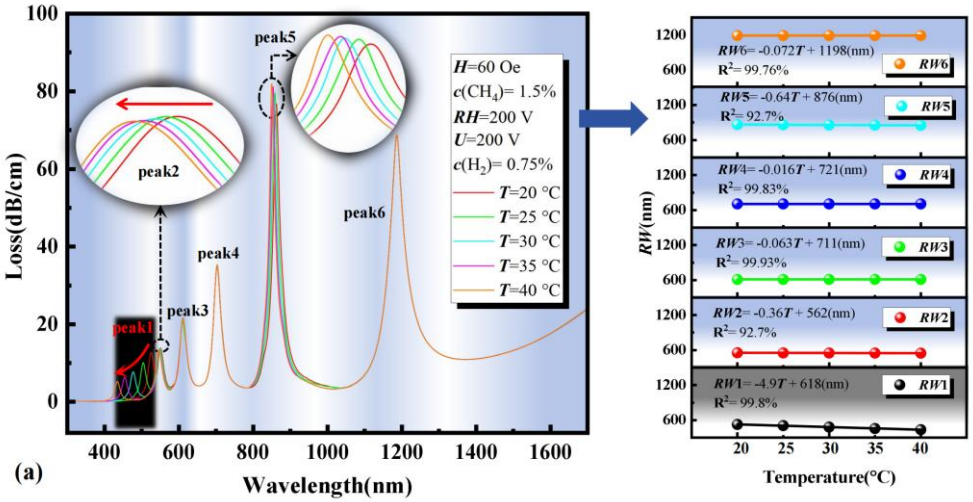


Fig. 10 (a) Loss spectra for *T* between 20 ºC and 40 ºC, and fitting results of the *RW* shift as a function of *T*.

Fig.10(b) shows the magnetic-field sensing characteristics of the optimized sensor. When the magnetic field varies in the range of 35 Oe-135 Oe, Peak 2 exhibits an obvious shift. Linear fitting is performed between the shift of each resonance peak and magnetic field, and the results are shown in Fig.11(b):

$RW1 = 0.003H + 487$(nm) ($R^2 = 99.85\%$); $RW2 = 0.85H + 501$(nm) ($R^2 = 96.78\%$);

$RW3 = 0.001H + 612$(nm) ($R^2 = 99.62\%$); $RW4 = 0.002H + 709$(nm) ($R^2 = 99.94\%$);

$RW5 = 0.22H + 847$(nm) ($R^2 = 99.27\%$); $RW6 = 0.002H + 1193$(nm) ($R^2 = 99.72\%$).

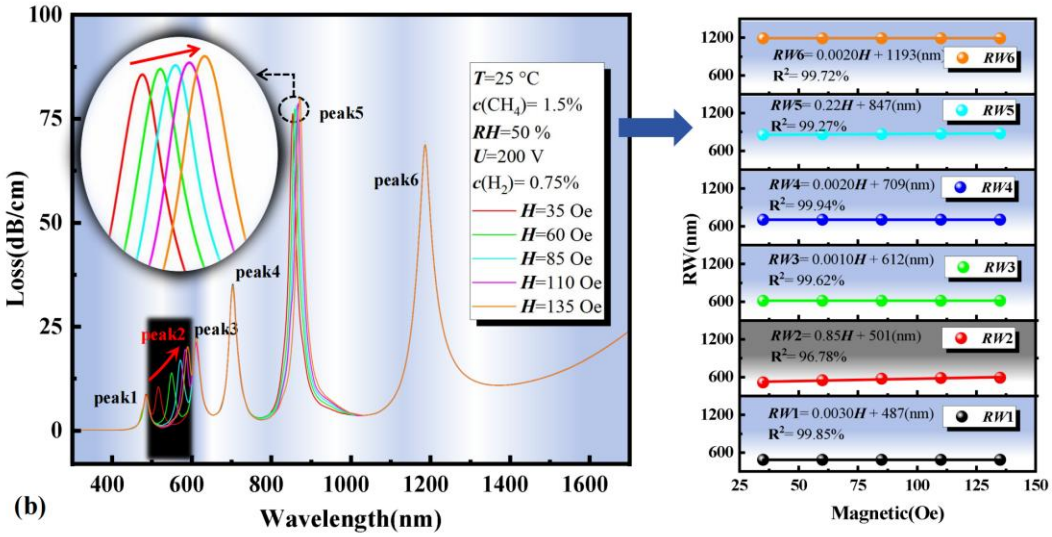


Fig. 10 (b) Loss spectra for *H* between 35 Oe and 135 Oe, and fitting results of the *RW* shift as a function of *H*.

Fig.10(c) shows the methane sensing characteristics of the optimized sensor. When the methane concentration varies in the range of 0%-2%, Peak 3 exhibits an obvious shift. Linear fitting is performed between the shift of each resonance peak and methane concentration, and the results are shown in Fig.11(c): $RW1 = -0.0011c(CH_4) + 488$(nm) ($R^2 = 99.73\%$); $RW2 = -0.0012c(CH_4) + 543$(nm) ($R^2 = 99.89\%$); $RW3 = -43c(CH_4) + 678$(nm) ($R^2 = 98.61\%$); $RW4 = 0.0019c(CH_4) + 704$(nm) ($R^2 = 99.42\%$); $RW5 = 0.0011c(CH_4) + 857$(nm) ($R^2 = 99.86\%$); $RW6 = 0.0082c(CH_4) + 1181$(nm) ($R^2 = 99.13\%$).

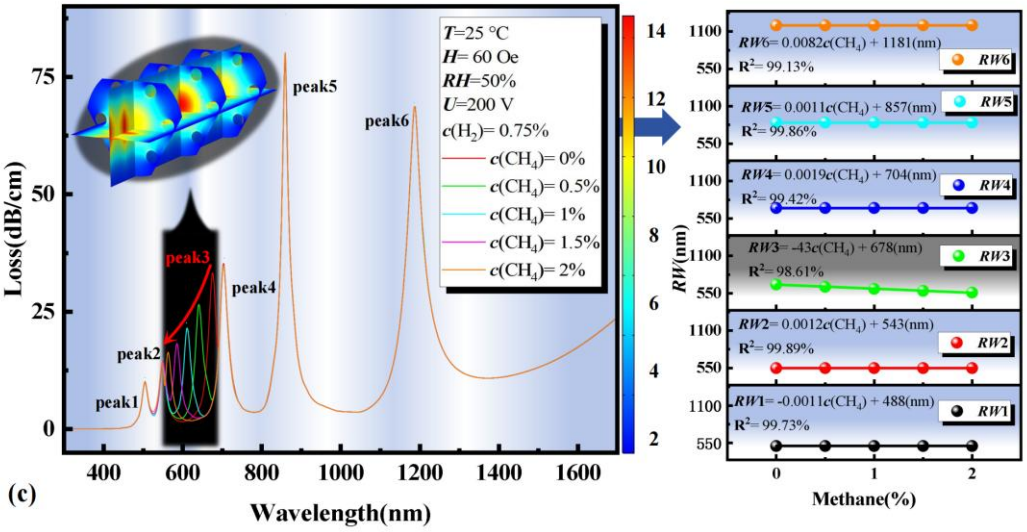


Fig. 10 (c) Loss spectra for $c(CH_4)$ between 0% - 2%, and fitting results of the *RW* shift as a function of $c(CH_4)$.

Fig.10(d) shows the relative-humidity sensing characteristics of the optimized sensor. When the relative humidity varies in the range of 30%-70%, Peak 4 exhibits an obvious shift. Linear fitting is performed between the shift of each resonance peak and relative humidity, and the results are shown in Fig. 11(d): $RW1 = 0.024RH + 472$(nm) (R^2 = 99.52%); $RW2 = 0.011RH + 537$(nm) (R^2 = 99.33%); $RW3 = 0.038RH + 603$(nm) (R^2 = 99.81%); $RW4 = -4.8RH + 934$(nm) (R^2 = 98.48%); $RW5 = 0.010RH + 852$(nm) (R^2 = 99.49%); $RW6 = 0.041RH + 1174$(nm) (R^2 = 99.89%).

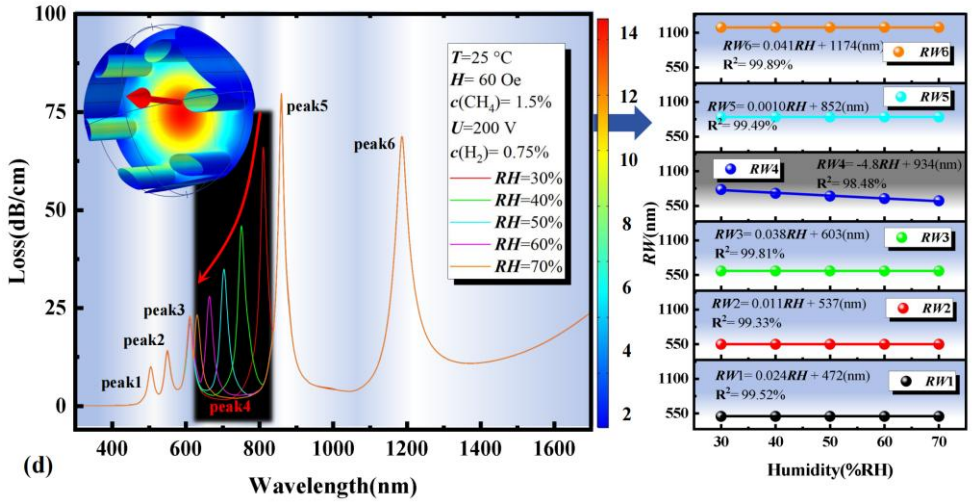


Fig. 10 (d) Loss spectra for *RH* between 30% - 70%, and fitting results of the *RW* shift as a function of *RH*.

Fig.10(e) shows the voltage sensing characteristics of the optimized sensor. When the voltage varies in the range of 180 V-260 V, Peak 5 exhibits an obvious shift. Linear fitting is performed between the shift of each resonance peak and voltage, and the results are shown in Fig.11(e): $RW1 = -0.054U + 498$(nm)($R^2 = 99.61\%$); $RW2 = -0.062U + 541$(nm)($R^2 = 99.72\%$); $RW3 = -0.0010U + 615$(nm)($R^2 = 99.93\%$); $RW4 = -0.0020U + 711$(nm)($R^2 = 99.66\%$); $RW5 = 4.0U + 101$(nm)($R^2 = 99.87\%$); $RW6 = -0.030U + 1198$(nm)($R^2 = 99.75\%$).

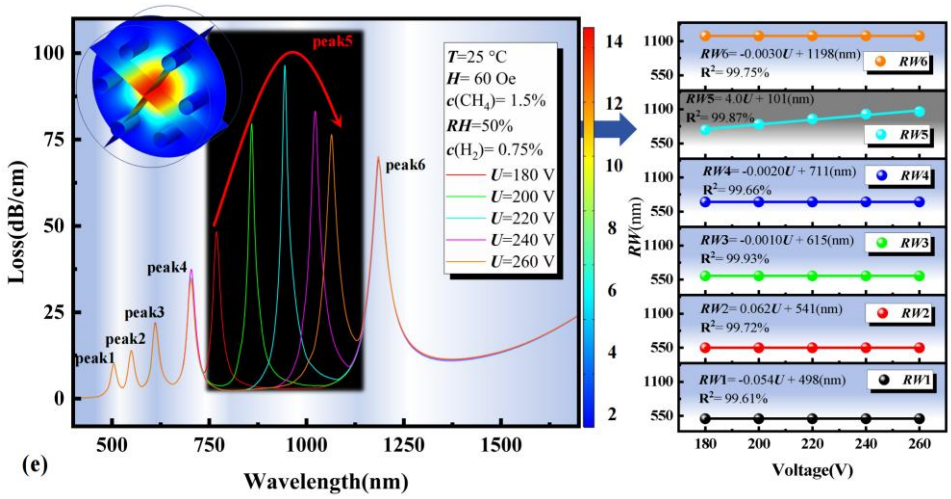


Fig. 10 (e) Loss spectra for *U* between 180 V - 260 V, and fitting results of the *RW* shift as a function of *U*.

Fig.10(f) shows the hydrogen sensing characteristics of the optimized sensor. When the hydrogen concentration varies in the range of 0%-3%, Peak 6 exhibits an obvious shift. Linear fitting is performed between the shift of each resonance peak and hydrogen concentration, and the results are shown in Fig.11(f): $RW1 = 0.0020c(H_2) + 462(nm)$ ($R^2 = 99.47\%$); $RW2 = 0.0010c(H_2) + 567(nm)$ ($R^2 = 99.73\%$); $RW3 = 0.068c(H_2) + 603(nm)$ ($R^2 = 99.82\%$); $RW4 = 0.0080c(H_2) + 688(nm)$ ($R^2 = 99.44\%$); $RW5 = 0.0040c(H_2) + 858(nm)$ ($R^2 = 99.13\%$); $RW6 = -60c(H_2) + 1233(nm)$ ($R^2 = 99.53\%$).

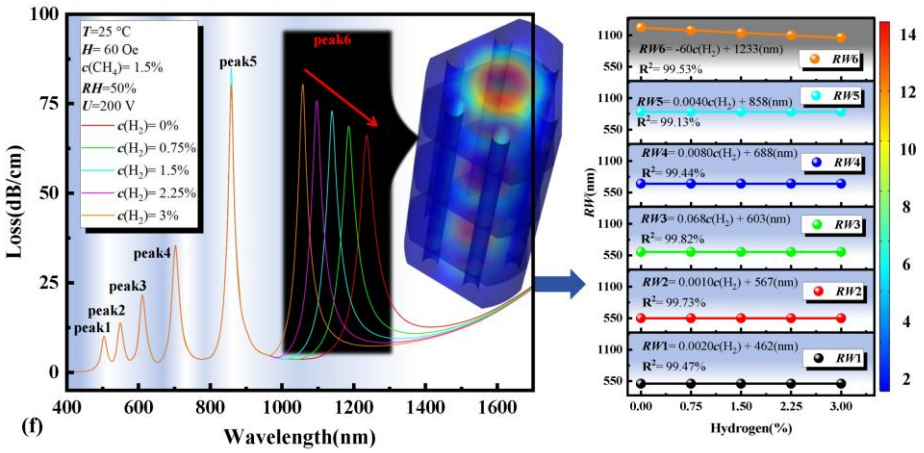


Fig. 10 (f) Loss spectra for $c(H_2)$ between 0% - 3%, and fitting results of the *RW* shift as a function of $c(H_2)$.

Substitute the sensitivity coefficients corresponding to the six resonance peaks calculated above into Equation (14), and perform matrix inversion to obtain the six-parameter sensing matrix as shown below. By measuring the shifts of the resonance peaks, the variation quantities of the six physical quantities can be demodulated.

$$\begin{bmatrix} \Delta T \\ \Delta H \\ \Delta c(\mathrm{CH_4}) \\ \Delta RH \\ \Delta U \\ \Delta c(\mathrm{H_2}) \end{bmatrix} =$$

$$\begin{bmatrix} -4.9\ \text{nm/°C} & 0.0030\ \text{nm/Oe} & -0.0011\ \text{nm/\%} & 0.024\ \text{nm/\%RH} & -0.054\ \text{nm/V} & 0.0020\ \text{nm/\%} \\ -0.36\ \text{nm/°C} & 0.85\ \text{nm/Oe} & -0.0012\ \text{nm/\%} & 0.011\ \text{nm/\%RH} & 0.062\ \text{nm/V} & 0.0010\ \text{nm/\%} \\ -0.063\ \text{nm/°C} & 0.0010\ \text{nm/Oe} & -43\ \text{nm/\%} & 0.038\ \text{nm/\%RH} & -0.0010\ \text{nm/V} & 0.068\ \text{nm/\%} \\ -0.016\ \text{nm/°C} & 0.0020\ \text{nm/Oe} & 0.0019\ \text{nm/\%} & -4.8\ \text{nm/\%RH} & -0.0020\ \text{nm/V} & 0.0080\ \text{nm/\%} \\ -0.64\ \text{nm/°C} & 0.22\ \text{nm/Oe} & 0.0011\ \text{nm/\%} & 0.0010/\text{\%RH} & 4.0\ \text{nm/V} & 0.0040\ \text{nm/\%} \\ -0.072\ \text{nm/°C} & 0.0020\ \text{nm/Oe} & 0.0082\ \text{nm/\%} & 0.041/\text{\%RH} & -0.0030\ \text{nm/V} & -60\ \text{nm/\%} \end{bmatrix}^{-1}$$

$$\cdot \begin{bmatrix} \Delta RW_1 \\ \Delta RW_2 \\ \Delta RW_3 \\ \Delta RW_4 \\ \Delta RW_5 \\ \Delta RW_6 \end{bmatrix} \begin{cases} 20\ ^\circ\mathrm{C} \le T \le 40\ ^\circ\mathrm{C} \\ 35\ \mathrm{Oe} \le H \le 135\ \mathrm{Oe} \\ 0\% \le c(\mathrm{CH_4}) \le 2\% \\ 30\% \le RH \le 70\% \\ 180\ \mathrm{V} \le U \le 260\ \mathrm{V} \\ 0\% \le c(\mathrm{H_2}) \le 3\% \end{cases}$$

The changes in the loss spectrum of the sensor under simultaneous variations of various environmental field quantities are numerically simulated, as shown in Fig.11(a). Each loss peak exhibits a regular shift. In addition, the electric-field distributions of the y-pol FM and SPP modes at the resonant wavelength are depicted in Fig.11(b). Independent coupling phenomena occur at all six gold-film positions, which verifies that the sensor can meet the requirements of multi-physical-field sensing.

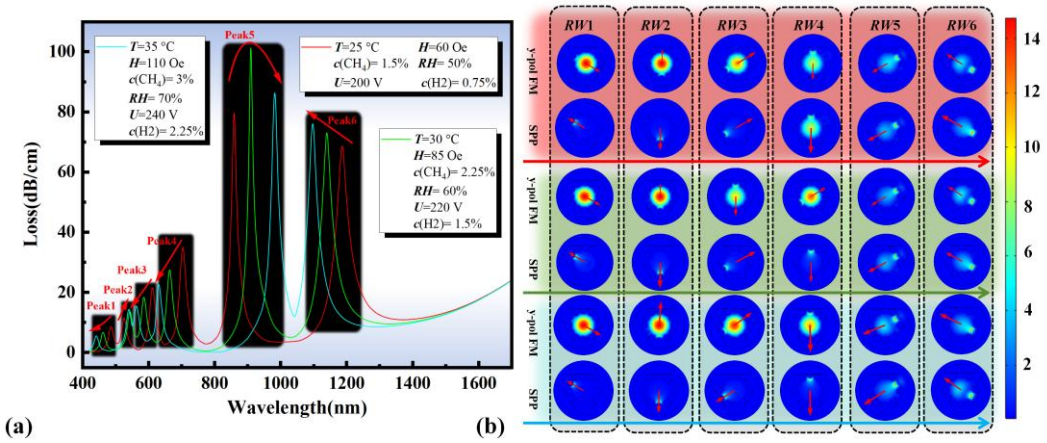


Fig. 11. When six field quantities vary simultaneously: (a) Loss spectra of y-pol FM; (b) Electric-field distributions of y-pol FM and SPP modes.

5. Discussion

5.1 Comparison of Sensing Performance

Table 1 compares the performance of different optical fiber sensors. By comparison, the proposed sensor realizes integrated detection of six physical quantities for the first time, and the sensitivities for each physical quantity are at a relatively high level.

Table. 1. Comparison of Sensing Performance of Different Multi-parameter Optical Fiber Sensors.

[30]	[9]	[11]	[31]	**This work**
$c(CH_4)$: 0%-2%	*T*: 10ºC-55ºC	*T*: 20ºC-40ºC	*N*: 1.32-1.38	*T*: 20ºC-40ºC
-4.03nm/%	-2.6nm/ºC	-13.8nm/ºC	4490nm/RIU	-4.9nm/ºC
$c(H_2)$: 0%-2%	*H*: 0mT-7mT	*H*: 35Oe-135Oe	*T*: 20ºC–40ºC	*H*: 35Oe-135Oe
-14.19 nm/%	1.77nm/Oe	1.86nm/Oe	-8.05nm/ºC	0.85 nm/Oe
	RH: 30%-80%	*RH*: 30%-70%	*H*: 35Oe-135Oe	$c(CH_4)$: 0%-2%
	-0.163nm/%RH	-5.1nm/%RH	1.52nm/Oe	-43nm/%
		U: 180V-260V	*RH*: 30%-70%	*RH*: 30%-70%
		5.24nm/V	-5.83nm/%RH	-4.8nm/%RH
			U: 180V-260V	*U*: 180V-260V
			4.25nm/V	4.0nm/V
				$c(H_2)$: 0%-3%
				-60nm/%

5.2 Condition Number

Substituting the sensitivity matrix into Formula 14 yields a condition number of cond(A) = 71.22. This value is far below the critical stability threshold, indicating that the matrix is well-conditioned. The parameter inversion method via matrix inversion is insensitive to measurement noise, the inversion calculation process is absolutely stable, and there is no risk of ill-conditioned divergence.

5.3 Fabrication Tolerance

Tolerance robustness analysis is carried out for the core structural parameters (d, l_1 and h) that determine sensing performance, and the sensitivity fluctuations of six sensing channels within the ±3% manufacturing error range are quantified. The results are shown in Table 2. When the structural parameters deviate from the design values within the typical manufacturing tolerance range of ±3%, the maximum sensitivity fluctuation of all channels is less than 6%. This result theoretically proves that the proposed structure has strong anti-fluctuation capability against manufacturing errors, and the sensor can maintain stable

sensing performance even if there are certain deviations of structural parameters between different preparation batches.

Table. 2. The Sensitivities When Some Parameters Vary within the Range of ±3%.

Param.	Tol.	$S_1(T)$ nm/ºC	$S_2(H)$ nm/Oe	$S_3(c(CH_4))$ nm/%	$S_4(RH)$ nm/%RH	$S_5(U)$ nm/V	$S_6(c(H_2))$ nm/%
	-3%	-4.91	0.83	-41.28	-4.82	3.91	-59.96
d	0	-4.92	0.85	-41.30	-4.85	3.95	-60.05
	+3%	-4.89	0.81	-41.26	-4.81	3.92	-60.01
	-3%	-4.91	0.79	-41.25	-4.88	3.91	-60.03
l_1	0	-4.92	0.85	-41.30	-4.85	3.95	-60.05
	+3%	-4.85	0.80	-41.26	-4.77	3.93	-60.02
	-3%	-4.90	0.91	-41.27	-4.78	3.88	-59.95
h	0	-4.92	0.85	-41.30	-4.85	3.95	-60.05
	+3%	-4.86	0.79	-41.22	-4.81	3.92	-59.96

6. Conclusion

A 6-parameter multi-physical field optical fiber sensor based on 12-hole fiber is designed, analyzed, and optimized for the simultaneous detection of temperature, magnetic field, methane, relative humidity, voltage and hydrogen. The sensor uses gold as the plasmonic medium to excite SPR, while PDMS, MF, Crypt-A/UVCFS, PVA, E7NLC, and Pd-WO_3 serve as the sensing materials for T, H, $c(CH_4)$, RH, U, and $c(H_2)$, respectively. The optimized structural parameters are d = 18.75 μm, l_1 = 40.625 μm, l_2 = 4.6875 μm, and h = 25 nm. Numerical analysis shows that in the temperature (20-40°C), magnetic field (35-135 Oe), methane concentration (0%-2%), relative humidity (30%-70%), voltage (180-260 V), and H_2 concentration (0%-3%) ranges, the average sensitivities of the sensor to temperature, magnetic field, methane, relative humidity, voltage, and hydrogen reach -4.9 nm/°C, 0.85 nm/Oe, -41.3 nm/%, -4.85 nm/%RH, 3.95 nm/V, and 60.05 nm/%, respectively. This sensor has a simple structure and achieves a

breakthrough in integration density in the field of optical fiber sensing. Comprehensive simulation data shows that this sensor exhibits excellent performance in terms of sensitivity, stability and repeatability, and can meet the usage requirements of complex industrial environments with strong coupling effects.

Funding

This work was jointly supported by the Heilongjiang Provincial Natural Science Foundation of China [JQ2023F001], National Natural Science Foundation of China [12304480], and Natural Science Foundation of Guangdong Province (2022A1515110971). The project was supported in part by the Fundamental Project Natural Science Foundation of Heilongjiang Province (LH2022F004) as well as City University of Hong Kong Donation Research Grants [DON-RMG 9229021 and 9220061].

Disclosures

The authors declare no conflicts of interest.

Data availability.

Data underlying the results presented in this paper are not publicly available at this time but may be obtained from the authors upon reasonable request.

References

[1] S. Liu, M. Xue, X. Cui, and W. Peng, "A review on the methane emission

detection during offshore natural gas hydrate production," Front. Energy Res., vol. 11, p. 1130810, 2023, doi: 10.3389/fenrg.2023.1130810.

[2] M. Fisser, R. A. Badcock, P. D. Teal, and A. Hunze, "High-sensitivity fiber-optic sensor for hydrogen detection in gas and transformer oil," IEEE Sens. J., vol. 19, no. 9, pp. 3348–3357, 2019, doi: 10.1109/JSEN.2019.2891523.

[3] J. E. Hall, P. Hooker, and K. E. Jeffrey, "Gas detection of hydrogen/natural gas blends in the gas industry," Int. J. Hydrogen Energy, vol. 46, no. 23, pp. 12555–12565, 2021, doi: 10.1016/j.ijhydene.2020.08.200.

[4] T. Wang, Z. Luo, H. Wen, F. Cheng, J. Deng, J. Zhao, et al., "Effects of flammable gases on the explosion characteristics of CH4 in air," J. Loss Prev. Process Ind., vol. 49, pp. 183–190, 2017, doi: 10.1016/j.jlp.2017.06.018.

[5] R. van Herel, R. Sinton, W. Enright, and P. Bodger, "Wire explosion by electromagnetic induction," IEEE Trans. Plasma Sci., vol. 40, no. 7, pp. 1891–1897, 2012, doi: 10.1109/TPS.2012.2198245.

[6] H. E. Joe, H. Yun, S. H. Jo, M. B. G. Jun, and B.-K. Min, "A review on optical fiber sensors for environmental monitoring," Int. J. Precis. Eng. Manuf. Green Eng., vol. 5, no. 1, pp. 173–191, 2018, doi: 10.1007/s40684-018-0017-6.

[7] P. Guo, K. Wang, H. Du, L. Zhang, J. Li, L. Huo, et al., "Spectrally-selective SPR fiber-optic sensor for simultaneous monitoring of glucose, pH, and temperature in biopharmaceutical processes," Opt. Laser Technol., vol. 196, p. 114645, 2026, doi: 10.1016/j.optlastec.2025.114645.

[8] R. C. Jorgenson and S. S. Yee, "A fiber-optic chemical sensor based on surface

plasmon resonance," Sens. Actuators B, Chem., vol. 12, no. 3, pp. 213–220, 1993, doi: 10.1016/0925-4005(93)80036-6.

[9] M. Wu, S. Pu, C. Zhang, W. Liu, S. Han, J. Fu, et al., "Triple-channel optical fiber surface plasmon resonance sensor for simultaneous detection of relative humidity, magnetic field, and temperature," IEEE Sens. J., vol. 24, no. 14, pp. 22439–22443, 2024.

[10] C. Liu, W. Wang, J. Lv, F. Wang, J. Wang, W. Liu, et al., "Coreless optical fiber sensor based on surface plasmon resonance for simultaneous measurement of magnetic field and temperature," IEEE Sens. J., vol. 25, no. 12, pp. 21581–21588, 2025, doi: 10.1109/JSEN.2025.3562485.

[11] W. Wang, J. Lü, J. Wang, F. Wang, W. Liu, X. Song, et al., "High-precision surface-plasmon-resonance-based four-parameter optical fiber sensor for simultaneous detection of temperature, magnetic field, relative humidity, and voltage," Chin. Opt. Lett., vol. 24, no. 3, p. 032601, 2026, doi: 10.3788/COL202624.032601.

[12] M. Shiraishi, K. Goya, M. Nishiyama, S. Kubodera, and K. Watanabe, "Femtosecond laser microhole drilling inside a fused silica optical fiber with optical inner surface quality," Appl. Phys. A, Mater. Sci. Process., vol. 122, no. 9, p. 825, 2016, doi: 10.1007/s00339-016-0352-9.

[13] W. Zhou, D. J. Mandia, M. B. E. Griffiths, S. T. Barry, and J. Albert, "Effective permittivity of ultrathin chemical vapor deposited gold films on optical fibers at infrared wavelengths," J. Phys. Chem. C, Nanomater. Interfaces, vol. 118, no.

1, pp. 670–678, 2014, doi: 10.1021/jp410937f.

[14] B. W. C. Au, K. Y. Chan, W. L. Pang, C. L. Lee, and A. H. Mustafa, "Tungsten oxide (WO_3) films prepared by sol-gel spin-coating technique," Diffus. Defect Data Solid State Data Pt. B, Solid State Phenom., vol. 280, pp. 71–75, 2018, doi: 10.4028/www.scientific.net/SSP.280.71.

[15] R. Xu, X. Li, W. Liu, J. Lv, L. Yang, J. Wang, et al., "Symmetrical dual-D and dual-core single-mode fiber surface plasmon resonance liquid sensor," J. Opt. Soc. Am. A Opt. Image Sci. Vis., vol. 41, no. 8, pp.1469–1478, Aug. 1 2024. DOI: 10.1364/JOSAA.525157.

[16] J. Wang, X. Lu, C. Mi, Q. Yin, J. Lv, L. Yang, et al., "Ultra-high sensitivity photonic crystal fiber sensor based on dispersion turning point sensitization of surface plasmonic polariton modes for low RI liquid detection," Opt. Express, vol. 32, no. 19, pp.32895–32908, Sep. 9 2024. DOI: 10.1364/OE.531112.

[17] S. Kim and X.-B. Pan, "Anisotropic nematic liquid crystals in an applied magnetic field," Nonlinearity, vol. 33, no. 5, pp.2035–2076, May 2020. DOI: 10.1088/1361-6544/ab7103.

[18] J. Korec, K. A. Stasiewicz, L. R. Jaroszewicz, W. Piecek, and P. Kula, "Temperature and voltage sensing based on a tapered optical fiber device with the liquid crystal cladding," (J), Opt. Fiber Technol., vol. 56, p.102190, 2020. DOI: 10.1016/j.yofte.2020.102190.

[19] H. Liu, C. Zhu, Y. Wang, C. Tan, and H. Li, "Polarization-dependent transverse-stress sensing characters of the gold-coated and liquid crystal filled

photonic crystal fiber based on surface plasmon resonance," (J), Opt. Fiber Technol., vol. 41, pp.27–33, 2018. DOI: 10.1016/j.yofte.2017.12.009.

[20] W. L. Wang, Q. Liu, Z. Y. Liu, Q. Wu, and Y.-Q. Fu, "Simulation of a temperature-compensated voltage sensor based on photonic crystal fiber infiltrated with liquid crystal and ethanol," (J), Sensors (Basel), vol. 22, no. 17, p.6374, 2022. DOI: 10.3390/s22176374.

[21] J. Li, S. T. Wu, S. Brugioni, R. Meucci, and S. Faetti, "Infrared refractive indices of liquid crystals," J. Appl. Phys., vol. 97, no. 7, p.073501, 2005. DOI: 10.1063/1.1877815.

[22] Z. Hao, Y. Li, S. Pu, J. Wang, F. Chen, and M. Lahoubi, "Ultrahigh-performance vector magnetic field sensor with wedge-shaped fiber tip based on surface plasmon resonance and magnetic fluid," Nanophotonics, vol. 11, no. 15, pp.3519–3528, Jul. 12 2022. DOI: 10.1515/nanoph-2022-0224.

[23] M. Song, X. Jing, P. Guo, Z. Yin, and S. Li, "SPR fiber optic sensor based on MMF-NCF doped with MgF2 for dual-parameter measurement of temperature and humidity," (J), Opt. Express, vol. 33, no. 2, pp.1869–1882, Jan. 27 2025. DOI: 10.1364/OE.541155.

[24] Z. Zhu, L. Liu, Z. Liu, Y. Zhang, and Y. Zhang, "Surface-plasmon-resonance-based optical-fiber temperature sensor with high sensitivity and high figure of merit," (J), Opt. Lett., vol. 42, no. 15, pp.2948–2951, Aug. 1 2017. DOI: 10.1364/OL.42.002948.

[25] J. Yang, L. Zhou, J. Huang, C. Tao, X. Li, and W. Chen, "Sensitivity enhancing

of transition mode long-period fiber grating as methane sensor using high refractive index polycarbonate/cryptophane A overlay deposition," Sens. Actuators B Chem., vol. 207, pp.477–480, 2015. DOI: 10.1016/j.snb.2014.10.013.

[26] J. Yang, L. Zhou, X. Che, J. Huang, X. Li, and W. Chen, "Photonic crystal fiber methane sensor based on modal interference with an ultraviolet curable fluoro-siloxane nano-film incorporating cryptophane A," Sens. Actuators B Chem., vol. 235, pp.717–722, 2016. DOI: 10.1016/j.snb.2016.05.125.

[27] Liu, Hai, et al. "D-shaped tellurite photonic crystal fiber hydrogen and methane sensor based on four-wave mixing with SPR effect."Photonic Sensors 13.1 (2023): 230121. DOI: 10.1007/s13320-022-0655-8.

[28] E. Gilbert, "Conditions for minimizing the norm sensitivity of characteristic roots," IEEE Trans. Automat. Contr., vol. 29, no. 7, pp.658–661, Jul. 1984., DOI: 10.1109/TAC.1984.1103608.

[29] T. Niu, G. Zhang, M. Zhang, and G. Zhang, "Joint inversion of gravity and gravity gradient data using smoothed L 0 norm regularization algorithm with sensitivity matrix compression," (J), Front. Earth Sci. (Lausanne), vol. 11, p.1283238, 2023. DOI: 10.3389/feart.2023.1283238.

[30] Liu, Hai, et al. "D-shaped tellurite photonic crystal fiber hydrogen and methane sensor based on four-wave mixing with SPR effect." Photonic Sensors 13.1 (2023): 230121. 10.1007/s13320-022-0655-8.

[31] W. Wang, J. Lv, J. Wang, M. Liu, W. Liu, Z. Yi, et al., "High-precision surface

plasmon resonance (SPR)-based five-parameter optical fiber sensor for the simultaneous detection of refractive index, temperature, magnetic field, relative humidity, and voltage," IEEE Sens. J., vol. 25, no. 24, pp. 44054–44062, 2025, doi: 10.1109/JSEN.2025.3627403.